ACS APPLIED NANO MATERIALS

www.acsanm.org Article

Eutectic Gallium−Indium Nanoparticles for Photodynamic Therapy of Pancreatic Cancer

Sabrina S. Hafiz,[§] Marvin Xavierselvan,[§] Sumeyra Gokalp,[§] Daniela Labadini, Sebastian Barros, Jeanne Duong, Michelle Foster,* and Srivalleesha Mallidi*

Cite This: *ACS Appl. Nano Mater.* 2022, 5, 6125−6139

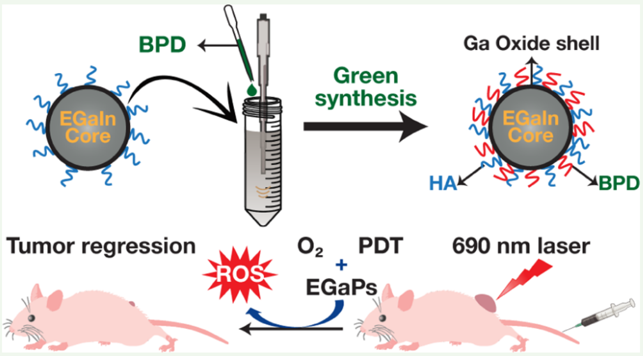

ABSTRACT: Developing a cancer theranostic nanoplatform with diagnosis and treatment capabilities to effectively treat tumors and reduce side effects is of great significance. Herein, we present a drug delivery strategy for photosensitizers based on a new liquid metal nanoplatform that leverages the tumor microenvironment to achieve photodynamic therapeutic effects in pancreatic cancer. Eutectic gallium indium (EGaIn) nanoparticles were successfully conjugated with a water-soluble cancer targeting ligand, hyaluronic acid, and a photosensitizer, benzoporphyrin derivative, creating EGaIn nanoparticles (EGaPs) via a simple green sonication method. The prepared sphere-shaped EGaPs, with a core−shell structure, presented high biocompatibility and stability. EGaPs had greater cellular uptake, manifested targeting competence, and generated significantly higher intracellular ROS. Further, near-infrared light activation of EGaPs demonstrated their potential to effectively eliminate cancer cells due to their single oxygen generation capability. Finally, from *in vivo* studies, EGaPs caused tumor regression and resulted in 2.3-fold higher necrosis than the control, therefore making a good vehicle for photodynamic therapy. The overall results highlight that EGaPs provide a new way to assemble liquid metal nanomaterials with different ligands for enhanced cancer therapy.

KEYWORDS: *liquid metal nanoparticles, EGaIn, photodynamic therapy, drug release, pancreatic cancer PDT*

1. INTRODUCTION

Adenocarcinoma of the pancreas is a malignant disease with less than a 10% survival rate.[1,2] The current mainstay of treatment for pancreatic cancer involves fractionated radiation and chemotherapy following surgical resection.[3,4] Despite treatment with chemotherapy and radiation therapy, pancreatic survival rates have remained low because of the anatomical location of the cancer resulting in inoperable surgery.[4] Furthermore, chemotherapy is associated with severe systemic toxicity. The need for a spatially localized therapy was fulfilled by photodynamic therapy (PDT), a spatiotemporally controlled technique, which has been recently shown to reduce pancreatic tumor volume in humans, making previously unresectable tumors resectable and also lead to an increase in median survival of 9.5 months after the treatment.[5−7]

The PDT mechanism of action involves activation of molecules called photosensitizers (PSs) in targeted tissues under the radiation of a specific wavelength generating cytotoxic reactive species including reactive oxygen species (ROS).[8] Compared to traditional radiation or chemotherapy, PDT features high disease specificity, leaving normal tissues unharmed.[5] Therefore, its therapeutic efficacy is relatively high with minimal side effects. However, the primary limitations include insufficient PS delivery, tumor-oxygenation dependency, and inaccurate dosimetry in aggressive tumors.[9,10] Additionally, conventional photosensitizers for PDT generally suffer from undesirable hydrophobicity and low bioavailability. Benzoporphyrin derivative (BPD), a highly efficient second-generation PS and FDA-approved PDT agent, has been well characterized for its therapeutic efficacy in *in vivo* cancer models.[11−14] The phase I/II study in patients with locally advanced unresectable pancreatic adenocarcinoma showed that BPD-based PDT treatment induced tumor necrosis and reduced tumor volume.[6,7] The strong absorption of BPD in the near-infrared (NIR) region at 690 nm promotes better tissue penetration of light as is appropriate for treating tumors in solid organs like the pancreas. Therefore, several strategies have been explored to develop PDT for effective disease treatment using nanoparticles as vehicles for conventional PSs,

Received: December 15, 2021
Accepted: April 12, 2022
Published: May 15, 2022

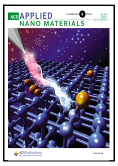

https://doi.org/10.1021/acsanm.1c04353

thus enhancing the bioavailability of these PS molecules.[13−17] Moreover, nanoparticles can also be modified with specific ligands to achieve active tumor targeting. Hyaluronic acid (HA) is one such tumor-targeting moiety that can bind to CD44 receptors that are over-expressed in several types of tumors, including pancreatic cancer and tumor-initiating stem cells.[18−23] The CD44 overexpression is implicated in tumor progression and enhanced metastasis, and it can specifically bind HA, thus making it an attractive receptor for targeted PDT.[24]

Various inorganic materials have been reported in recent years as photodynamic agents or carriers and have been reviewed extensively elsewhere.[9,25,26] Many of these particles such as gold nanoparticles, semiconductor nanoparticles, hydrogel nanostructures, and polymer composites are used not only for delivery of the photosensitizer but also to enhance PDT efficacy through photocatalytic mechanisms for applications involving cancer and infectious diseases.[27−30] For example, gold nanoparticles have attracted much attention as good optical contrast agents and also carriers of PSs due to their excellent photochemical, surface properties, and simple thiolation chemistry for the functionalization of desired molecules, thus enhancing their capability for loading PS drugs.[30−33] Semiconductor hybrid nanostructures containing Ag/Ag@AgCl/ZnO exhibit excellent photocatalytic activity and demonstrate highly effective antibacterial activity under visible light irradiation.[34] They showed that incorporation of Ag/Ag@AgCl nanostructures enhanced the photocatalytic and antibacterial activity of ZnO due to the enhancement of reactive oxygen species by visible light. Xiang et al. developed semiconductor heterojunctions of ZnO/CDots/C_3N_4 with enhanced photocatalytic efficiency to kill bacteria effectively within a very short time under the irradiation of visible light.[35] These studies point to the potential inorganic nanoparticles have in delivering PS to tumors for PDT due to high surface-to-volume ratio, chemical inertness, photocatalytic properties, bioconjugation, and broad optical properties.[36,37] However, they need to be engineered specifically to respond under low pH cancer cellular conditions, involve complex fabrication procedures, and are generally not biocompatible with agglomeration in the liver, spleen, and at the tumor site.[38] Lately, the focus on the advancement of gallium-based liquid metals such as eutectic gallium indium (EGaIn, 75% Ga, 25% In) nanoplatforms for therapy, imaging, and biosensing of cancers has increased due to their unique tunable properties, which can be manipulated by the surrounding environment.[12,39,40] They rapidly form a thin passivating oxide layer on their surface when exposed to oxygen,[41] which presents opportunities to synthesize nanomaterials with engineered surface properties, thus paving the way for a variety of biomedical applications. Researchers have shown that liquid metal nanoparticles can rapidly heat up and produce reactive oxygen to deform and release the drug under NIR radiation.[42−44] The usage of EGaIn in the biosystem is relatively new but is gaining much attention since it has shown a wide range of benefits, such as low cytotoxicity, biocompatibility, photocatalytic activity, and high conductivity.[45] Therefore, EGaIn nanoparticles are suitable candidates as theranostic agents. Functionalizing the oxide skin with drugs and targeting agents can create a promising and novel system for drug delivery. The oxide surface of EGaIn will degrade in the mild acidic microenvironment of the endosomes promoting acid-triggered drug release.[46] Furthermore, gallium itself is an anticancer agent and can reverse drug resistance in drug-resistant cancer cells.[47] Moreover, these nanoparticles have a liquid core that leads to fewer reactive sites after the dissolution of the oxide skin and can reduce their potential systemic toxicity. In fact, a study has shown that EGaIn nanoparticles modified with a water-soluble polymer showed higher cell viability than gold nanoparticles and carbon nanotubes.[44]

Recent progress using EGaIn nanoparticles for diverse therapeutic applications concentrates on the formulation of EGaIn nanoparticles and their biofunctional moieties, which influence their properties and performance.[42,44,46,48−50] To date, many thiolated ligands such as cyclodextrin, HA, and poly(ethylene glycol) have been used as capping agents to form systemically stabilized EGaIn nanoparticles.[42,46] However, due to the photolabile characteristics of thiols and their ability to inactivate metalloenzymes in living organisms, they can cause unwanted side effects and toxicity.[51] Our previous work showed the synthesis of stabilized core−shell EGaIn nanoparticles in carboxylic acids in which the carboxylate group was chemically bound to the oxide layer.[52,53] Since, both HA and BPD contain carboxylic groups, they can covalently bind directly to the surface of EGaIn forming carboxylate bonds. In this work, we presented a "green" nanoformulation strategy to construct multifunctional EGaIn nanoparticles having advantageous morphology, favorable biocompatibility, splendid versatility, and the ability to deliver drugs for anticancer therapy. Specifically, we illustrated a synthesis process that is simple, highly reproducible, and inexpensive for the production of stable, PS- and HA-coated EGaIn nanoparticles. We report the surface chemistry, namely, the functionalization of EGaIn nanoparticles with BPD and HA to fabricate EGaPs and the stability of the produced nanoparticles through various spectroscopic techniques. The use of a targeting ligand resulted in improved cellular uptake and internalization of the PS. The inherent dark toxicity and PDT effectiveness of EGaPs were demonstrated *in vitro* with multiple pancreatic cancer cell lines. Finally, *in vivo* studies with the pancreatic cancer xenograft murine model revealed that EGaP-based PDT significantly inhibited tumor growth suggesting an adaptive therapeutic influence. This study confirms the versatility of EGaIn nanoparticles functionalized with both PS and targeting ligands that can be utilized for enhanced cancer therapy.

2. EXPERIMENTAL SECTION

2.1. Materials. Gallium−indium eutectic (≥99.99% trace metal basis), BPD-benzoporphyrin derivative monoacid ring A (≥94%), hyaluronic acid sodium salt from *Streptococcus equi* (molecular weight: 130,000−150,000), and Dulbecco's phosphate buffer solution (PBS) were purchased from Sigma-Aldrich. Dimethyl sulfoxide (DMSO), muscovite mica V-2 (50-949-111), and conical polypropylene centrifuge tubes (05-539-9LC) were obtained from Thermo Fisher Scientific. Throughout all of the experiments, deionized (DI) water with a resistivity of 18.2 MΩ·cm was used.

2.2. Fabrication of Stable Targeted EGaIn Nanoparticles Loaded with Photosensitizers. EGaIn nanoparticles loaded with PSs were synthesized with BPD and HA (EGaPs). HA, a water-soluble ligand, was chosen as a surface ligand due to its multifunctional nature, acting not only as a targeting moiety but also as a stabilizing agent.[54] In synthesizing EGaPs, the first liquid EGaIn was sonicated in an aqueous solution of HA to create HA-coated EGaIn nanoparticles (EGaIn-HA). Thirty microliters of EGaIn was used as received. EGaIn was added to a 50 mL centrifuge tube, which contained 1 mg of HA (0.1 mg/mL) in 10 mL of deionized

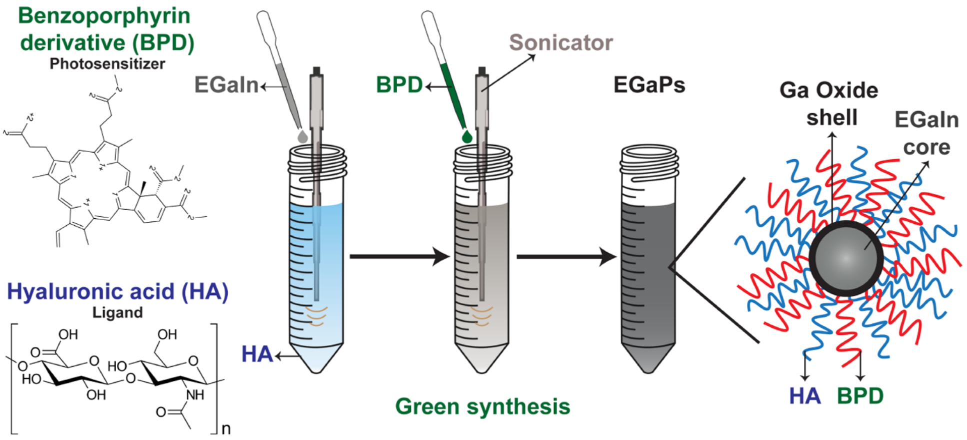

Figure 1. Schematic depiction of the protocol to fabricate stable EGaPs.

water. The centrifuge tube was placed in a water bath and the solution was sonicated for 75 min by a probe sonicator (Qsonica Q125) with 50% amplitude. The sonication conditions were used with a pulse 59 s and a pause 1 s to avoid the heating of nanoparticles. After sonication, the large particles in the resulting suspension were removed by mild centrifugation (rotating speed of 1000 rpm). The supernatant containing EGaIn-HA was further purified by centrifugation with a speed of 4700 rpm and washed with DI water three times. Finally, EGaIn-HA was resuspended in the PBS buffer.

To synthesize EGaPs, 30 μL of EGaIn was added to a 50 mL polypropylene tube, which contained 1 mg of HA in 7.6 mL of water. The centrifuge tube was placed in an ice water bath to prevent heating of nanoparticles and the solution was sonicated for 75 min by a probe sonicator with 50% amplitude. The sonication conditions were used with a pulse 59 s and a pause 1 s to avoid the heating of nanoparticles. Once the sonication is complete, 2.4 mL of BPD with a concentration of 300 μM in DMSO solution was added to the EGaIn-HA slurry solution and further sonicated for 1 h to produce EGaPs. The large particles in the resulting suspension were removed by mild centrifugation, at a speed of 1000 rpm. The supernatants containing EGaPs were further purified by centrifugation at a speed of 4700 rpm and washed with DI water three times. Finally, EGaPs were resuspended in the PBS buffer. The EGaPs were stored at 4 °C. The color of the suspension changed from gray to dark greenish-gray once the BPD was loaded onto the surface of EGaIn-HA (Figure S1a,b). The dark color of the solution indicates that highly concentrated, stable nanoparticles are formed. The preparation route of EGaPs is illustrated in Figure 1.

2.3. Atomic Force Microscopy (AFM).

For AFM sample preparation, 2 μL of EGaP solutions was dropped on the freshly cleaved mica surface. The sample was left to air dry for 30 min and then rinsed with deionized water. The excess deionized water was gently removed by tapping with a corner of a Kimtech wipe. AFM measurements were performed with a Bruker Innova AFM under ambient conditions. The microscope was placed on an air table to minimize vibrational noise. All measurements were performed in the taping mode. Silicon probes (Bruker) with a spring constant of 42 Nm^{-1} were used. The AFM tips were made from silicon with a 30 nm aluminum coating. The topographical images were recorded at 512-line resolution. The morphological structures of EGaPs were further processed using NanoScope Analysis 1.9 software (Bruker) to determine the diameter of the individual EGaPs. A total of 200 nanoparticles were traced and analyzed.

2.4. Scanning Electron Microscope (SEM).

A Zeiss Ultra Plus Field Emission SEM was used to examine the nanostructure of the formed EGaPs on a carbon wafer substrate. Samples were imaged using an electron beam accelerating voltage of 5 kV and a working distance of 2.8−3.2 mm. Images were collected using an in-lens detector. The diameters of 200 nanoparticles from SEM images were analyzed using Smart TiffV3 software (Zeiss).

2.5. Dynamic Light Scattering (DLS).

DLS (Horiba SZ-100-HZ with a fixed angle dispersion of 90°) was used to measure the ζ potential, hydrodynamic diameter, polydispersity index (PDI), and ζ potential of the EGaPs. Polystyrene cuvettes with an optical path length of 1 cm (Sarstedt) filled with 100-fold diluted EGaP solution in PBS were used. The data reported are an average of three separate measurements.

2.6. Fluorescence Spectroscopy.

For fluorescence measurements, EGaPs were diluted 100-fold in DMSO in a 96-well black-walled flat-bottom plate. A SpectraMax i3X multimode plate reader (Molecular Devices) in top-read mode was used to measure EGaP fluorescence. An excitation wavelength of 420 nm and an emission wavelength range of 600−800 nm were used. The results reported were the average of three separate measurements.

2.7. Diffuse Reflectance Infrared Fourier Transform Spectroscopy (DRIFTS).

DRIFTS spectra (128 scans, 2 cm^{-1} resolution) were collected using Nicolet iS 50 FTIR spectrometers (Thermo Fisher Scientific, MCT-High D* detector) equipped with a Praying Mantis diffuse reflectance accessory (Harrick Scientific). The Praying Mantis accessory was situated inside the sample compartment of the FTIR, which was under constant N_2 purge. The EGaPs were dropped cast on a KBr powder-filled sample cup and spectra were collected from 750 to 4000 cm^{-1}.

2.8. Raman Spectroscopy.

Raman measurements were performed with a Bruker SENTERRA confocal Raman Microscope in air using a 532 nm laser, 6.25 mW of laser power, and 9−15 cm^{-1} resolution. The light was focused an approximately 2 μm spot using a 50× objective and a slit aperture of 50 × 1000 μm. The XYZ movement was controlled accurately using a motorized stage. Raman signals for clusters of EGaPs were collected at multiple spots using a 10 s integration time and 5 coadditions at each selected spot to increase the signal-to-noise ratio. Spectra were collected in the wavenumber range of 45−4450 cm^{-1}.

2.9. UV−visible Spectroscopy.

UV−visible absorption spectrophotometry was performed using a Cary UV−visible spectrophotometer (Agilent Technologies) with a double beam setup and a PbSmart detector, with a spectral bandwidth of 2 nm and a scan rate of 600 nm/min. Samples were put into quartz cuvettes, and the absorbance was measured from 175 to 800 nm.

2.10. Drug Release from EGaPs.

The controlled release of BPD from EGaPs was performed by incubating the samples in glycolic acid buffer of pH 6, 7.4, and 9 at 37 °C. The time points were set at 0, 6, 24, and 96 h. At each time point, the samples were centrifuged at 4700 rpm for 5 min and the concentration of free BPD in the supernatant was determined by UV−visible absorption spectrophotometry. The controlled release rate of BPD at different pH values was compared.

2.11. Photochemical and Photophysical Characterizations.

Singlet oxygen measurements were performed in a 96-well, black-walled, transparent bottom plate. Solutions of 1 μM free BPD (stock in DMSO) or EGaPs were prepared either in PBS or in glycolic acid (pH 6) and incubated at 37 °C for 1 or 24 h. The solutions (190 μL) were mixed with 10 μL of 50 μM Singlet Oxygen Sensor Green (SOSG; Thermo Fisher Scientific) prior to light irradiation. The solutions were irradiated with a 690 nm laser (HPD 7401; High Power Devices, Inc.) at an irradiance of 50 mW/cm^2 with fluencies of 0, 1, 2.5, 5, 10, and 20 J/cm^2. Therefore, the cumulative doses received by the wells are 0, 1, 3.5, 8.5, 18.5, and 28.5 J/cm^2. Following each individual dose application, the fluorescence intensity of SOSG was measured using a Synergy H1 microplate reader (BioTek) with an excitation of 460 nm and a collecting emission at 530 nm. The thermal response of EGaPs when irradiated with a 690 nm laser was investigated using a thermocouple-based oxygen/temperature bare-fiber sensor (OxyLite system; Oxford Optronix). The EGaPs, EGaIn-HA, and free BPD samples (1 mL; EGaIn concentration: 6085 μg/mL; BPD concentration: 45 μM) were irradiated in a 4 mL polystyrene cuvette (Sarstedt) for 30 min. The temperature of the solution was recorded at regular intervals and the experiment was performed in triplicates.

2.12. Cell Culture. AsPC-1 (pancreatic cancer derived from ascites) and MIA PaCa-2 cells (pancreatic ductal adenocarcinoma) were obtained from ATCC (American Type Culture Collection). AsPC-1 cells were maintained in the Roswell Park Memorial Institute 1640 (RPMI) medium with L-glutamine (Gibco), while MIA PaCa-2 cells were cultured in Dulbecco's modified Eagle's medium (DMEM). All media were supplemented with 10% fetal bovine serum (Gibco) and 1% Penicillin/Streptomycin (1:1 v/v, Corning), and cells were maintained in a humidified incubator at 37 °C and 5% CO_2.

2.13. Cellular Uptake of EGaPs. For evaluating EGaPs' cellular uptake, AsPC-1 and MIA PaCa-2 cells at 70−90% confluence were seeded in a 24-well plate at a density of 50,000 cells per well and incubated with free BPD or EGaPs at a concentration of 0.25 μM of BPD equivalent for 0, 1, 2, 4, 6, and 24 h. Cells were washed with ice-cold PBS and lysed using 2% Triton X-100 at 4 °C. BPD fluorescence was measured using a Synergy H1 microplate reader (BioTek) with appropriate standard solutions facilitating fluorescence intensity to be converted to moles of BPD. Protein concentration was quantified using a bicinchoninic acid protein assay kit (Millipore Sigma). To verify the EGaP internalization and uptake using fluorescence imaging, AsPC-1 and MIA PaCa-2 cells at 70−90% confluence were seeded in 35 mm glass-bottom dishes (MatTek Corporation) at a density of 50,000 cells per dish and incubated with 1 μM free BPD or EGaPs for 1, 2, 4, 6, and 24 h. Before imaging, cells were washed with PBS and nuclei were stained with Hoechst 33342 (2 μg/mL; Thermo Fisher Scientific). Live-cell imaging was performed using an EVOS M7000 imaging system (Invitrogen) using a 40× objective. Hoechst and BPD were imaged with a DAPI light cube and Qdot 705 light cube, respectively. The fluorescence images were processed using ImageJ software.

2.14. CD44 Expression and Targeting of EGaPs in Pancreatic Cancer Cells. For examining the CD44 expression, MIA PaCa-2 and AsPC-1 cells were seeded in 35 mm glass-bottom dishes at a density of 50,000 cells per dish and incubated overnight at 37 °C and 5% CO_2. The cells were then fixed with 4% paraformaldehyde for 15 min and permeabilized with 1% Triton X-100. Cells were then incubated with the primary antibody (anti-CD44, Invitrogen) overnight at 4 °C. Following the incubation, cells were stained with a fluorescent dye-tagged secondary antibody (Invitrogen) for 1 h at room temperature. Cells were counterstained with Hoechst 33342 (2 μg/mL) and visualized using an EVOS M7000 imaging system. The fluorescence images were processed using ImageJ. To investigate the targeting ability of EGaPs, MIA PaCa-2 cells were seeded in 35 mm glass-bottom dishes at a density of 50,000 cells per dish and incubated overnight. Prior to incubating with 1 μM EGaPs for 1 h, cells were incubated with or without 1 mg/mL of free HA for 4 h. Cells were counterstained with Hoechst 33342 (2 μg/mL) and imaged using an EVOS M7000 imaging system. Image processing was performed using ImageJ.

2.15. In Vitro Cytotoxicity of EGaPs. To evaluate the cytotoxicity (no light) of EGaPs, AsPC-1 cells were seeded in a 24-well plate at a density of 50,000 cells per well. The following day, cells were incubated with varying concentrations of free HA or EGaIn-HA for either 1 or 24 h. Following the incubation, media is replaced with fresh media and cells were incubated for a further 24 h prior to performing the viability assay using 3-(4,5-dimethylthiazol-2-yl)-2,5-diphenyltetrazolium bromide (MTT, Thermo Fisher Scientific). The media was replaced with fresh cell culture media containing MTT (0.25 mg/mL) and incubated for 1 h at 37 °C. The formazan crystals formed inside the cells were dissolved using DMSO and the absorbance was recorded at 570 nm using a Synergy H1 microplate reader (BioTek). Cell viability was calculated as a percentage absorbance at 570 nm with respect to untreated controls.

2.16. Intracellular ROS Evaluation. To evaluate the intracellular ROS production by EGaPs and free BPD, MIA PaCa-2 cells were seeded in 35 mm glass-bottom dishes at a density of 50,000 cells per dish. After 24 h of seeding, the cells were incubated with a 0.25 μM concentration of BPD equivalent to EGaPs for 1 h. Following the incubation, media was exchanged for fresh media and PDT was performed with a 690 nm laser at an irradiance of 50 mW/cm^2 with fluencies of 0 and 1 J/cm^2. After irradiation, intracellular ROS was detected using an Image-iT LIVE Green Reactive Oxygen Species Detection Kit (Invitrogen) as per the manufacturer's instructions. For the experimental control, ROS was induced by incubating cells with 200 μM tert-butyl hydroperoxide (TBHP) for 1 h. Briefly, cells were incubated with 5-(and-6)- carboxy-2′,7′-dichlorodihydrofluorescein diacetate (carboxyH_2DCFDA) for 30 min at 37 °C. Following the incubation, cells were washed with PBS and imaged with a 40× objective using an EVOS M7000 imaging system to visualize intracellular ROS. Image analysis was performed using ImageJ.

2.17. Photodynamic Therapy of Pancreatic Cancer Cells Using EGaPs. For the PDT study, AsPC-1 and MIA PaCa-2 cells were seeded in 35 mm Petri dishes at a density of 1×10^5 cells per dish. The following day, cells were incubated with s 0.25 μM concentration of BPD equivalent to EGaPs for 24 h. As a control, 0.25 μM free BPD or EGaPs incubated for 1 h were included as well. Following incubation, media was replaced with fresh culture media and cells were irradiated with a 690 nm laser at an irradiance of 50 mW/cm^2 with fluencies of 0, 1, 2.5, 5, and 10 J/cm^2. Cell viability was determined at 24 h after irradiation using an MTT assay as described in the previous section

2.18. In Vivo Therapy Efficacy of EGaPs. Animal experiments were performed in compliance with the Institutional Animal Care and Use Committee (IACUC) of Tufts University. Foxn1^{nu} mice were raised in aseptic conditions in the institution's animal facility with 12 h light and dark cycles. AsPC-1 cells at 80−90% confluence were trypsinized, collected, and suspended in a 1:1 v/v mixture of Matrigel and PBS at a density of 5×10^6 cells per 100 μL and injected subcutaneously in the mice. When the tumors reached an average size of ∼50 mm^3, either EGaPs or liposomal BPD at a dose of 0.5 mg/kg equivalent to BPD was administered to mice via tail vein injection. After a drug light interval of 90 min, PDT was performed with a 690 nm laser with an irradiance of 75 mW/cm^2 and a fluence of 200 J/cm^2. After PDT, the tumor volumes were monitored biweekly with ultrasound imaging for 30 days. Few tumors from each treatment group were euthanized on 48 h after PDT, and hematoxylin and eosin (H&E) staining was performed to visualize the damage caused to the tumors by EGaPs and liposomal BPD.

3. RESULTS AND DISCUSSION

3.1. Size Analysis of EGaPs. The synthesis of biostable and biocompatible liquid metal nanoparticles, EGaPs, was easily achieved using high-power sonication.[55] The one-step sonication process, using probe activation, breaks up the bulk EGaIn liquid into small nanoparticles with a coating of HA on the oxide layer acting as a stabilizing agent, producing stable liquid metal nanoparticles by lowering the surface tension.[55] The carboxylic acid groups of HA and BPD chemically react with the gallium oxide surface of EGaIn and adsorb covalently to the surface.[52] Thus, we developed a novel yet a simple and

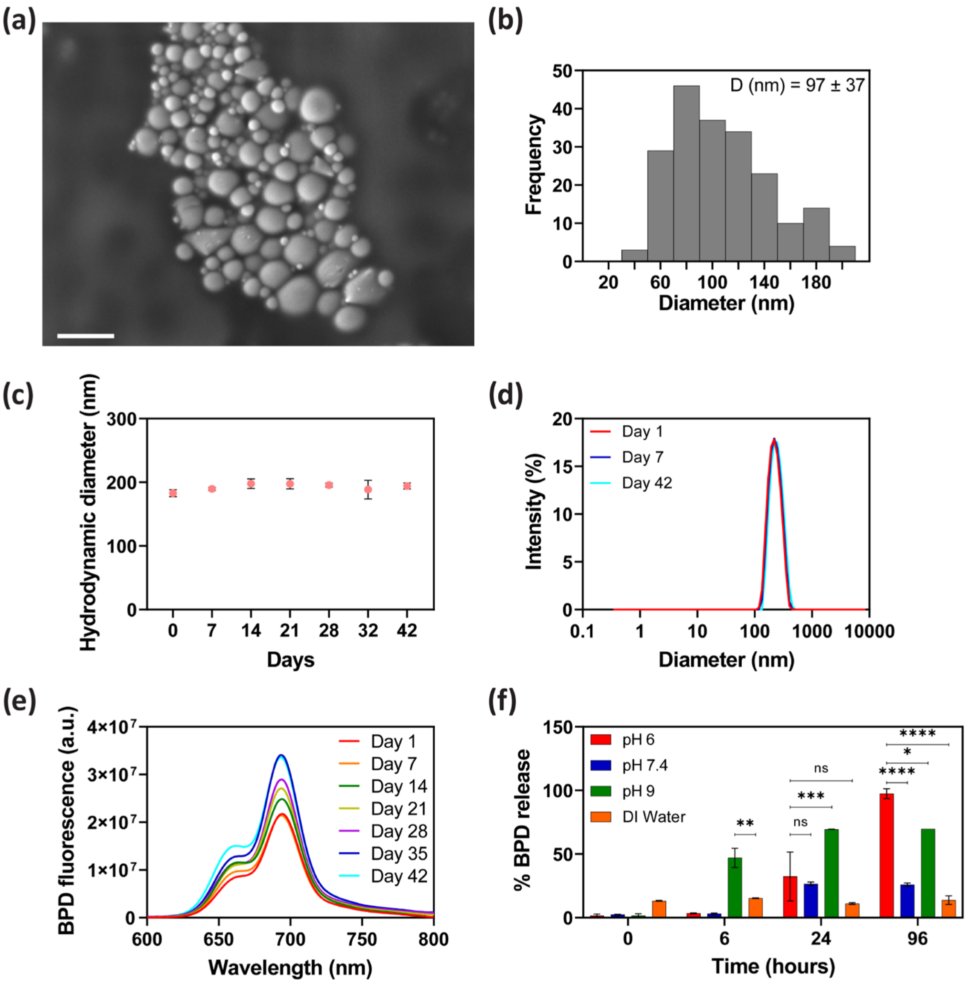

Figure 2. (a) SEM image of EGaPs. (b) Size distribution of 200 EGaPs measured with SEM images. (c) DLS measurements of EGaPs up to 6 weeks. (d) Temporal distribution plots from DLS measurements on Day 1, 7, and 42. (e) Fluorescence measurements of EGaPs as a function of time for 6 weeks. For (a), scale bar = 180 nm. For (c), the results are expressed as mean ± standard deviation ($n = 3$) and are not significant; One-way ANOVA with Tukey's multiple comparison test: $p > 0.05$. For (f), the results are expressed as mean ± standard error ($n = 6$; two experiments with three replicates each). Two-way ANOVA with Tukey's post hoc test; ns = $p > 0.05$, * = $p < 0.05$, ** = $p < 0.01$, *** = $p < 0.001$, and *** = $p < 0.0001$.

convenient synthetic method for creating stable EGaPs with core−shell structure, for the targeted delivery of the PS for PDT of pancreatic tumors. This fabrication methodology with one-step sonication involves no harsh chemicals and is safer and greener than other methods for preparing metal nanoparticles and liposomes.[52,56] The core−shell structure of EGaIn nanoparticles consists of the EGaIn metal alloy core with the gallium oxide layer bound with BPD and HA as the shell and it has been previously reported.[42,43,49,57] Further analysis was performed with AFM, SEM, and DLS to better understand the structure, shape, size distribution, and stability of EGaPs.

The size of the nanoparticles is an important factor in drug delivery, as nanoparticles smaller than 10 nm can be easily cleared by the kidneys, while larger nanoparticles need to overcome the reticuloendothelial system.[58−61] Nanoparticles within the range of 20−200 nm were shown to have a higher chance to accumulate at tumor sites due to leaky tumor vasculature, making them ideal for drug delivery.[62−64] From the AFM images shown in Figure S2a, the bright yellow, smooth spherical structures represent individual EGaPs, while the brown featureless surface represents the mica substrate. A total of 20−25 images were collected from different areas of the sample and were used to determine the size distribution of 200 EGaPs. Obvious agglomerates were excluded from the analysis. Since the particles are spherical, height measurements were used to determine particle diameters. The histogram in Figure S2b illustrates the size-distribution analysis of 200 different EGaPs, giving an average diameter of 38 ± 10 nm and a size range of 25−65 nm. Figure 2a depicts the SEM image of EGaPs taken under vacuum, and the spherical structure of the nanoparticles is clearly still intact and visible. The diameters of 200 EGaPs were determined using 5−10 SEM images. The histogram of the size distribution from SEM images shows that the average size of the EGaPs is 97 ± 37 nm with a range of 30−210 nm (Figure 2b).

HA- and BPD-coated EGaIn nanoparticles were nanospheres as confirmed by both AFM and SEM. Visually, no difference in the morphologies of EGaPs was observed in the AFM and SEM images. However, the calculated diameters of the nanoparticles from SEM images were higher (more than doubled) than those determined from AFM size analysis. The AFM methodology is considerably different than SEM as it provides a 3D topographical image, which is used to determine the height as the diameter in the z-direction.[65−67] One of the main factors that may explain the size difference is that AFM analysis of EGaPs is done by selecting particles individually, while the SEM software measures the diameter of all particles within an image without individual selection. Another factor is that EGaPs might be flattened (wetting the surface of the substrate) due to the presence of the oxide layer, which would reduce the height and increase the width.[68] One potential issue with SEM is that as $x-y$ distances are used for particle diameter calculation, the lateral magnification becomes important. On AFM, lateral magnification is not an important factor since dimensions (height) are measured on the z-axis, and with lower levels of noise and higher resolution, it is a better measurement technique for nanoparticles of any size. Overall, SEM and AFM techniques are complementary to each other,[65] and both methods show that the average diameter is well within the 20−200 nm range needed for effective nanocarriers.

DLS was used to evaluate the hydrodynamic diameter of the EGaPs in solution. Figure 2c presents the results of DLS measurements taken with 100-fold diluted EGaPs in PBS, showing an average diameter of 182 ± 8 nm. This result indicates that the hydrodynamic diameter of EGaPs is greater than the size distribution obtained from either AFM or SEM. It is important to note that DLS takes a different approach to size analysis where an average size is determined by the intensity of the light scattering when the particles are in the solution.[69] Since light scattering measures not only the hydrodynamic diameter of the particles but also the ionic and solvent layers within the solution, it is not appropriate to directly compare DLS with microscopic measurements.[67] Typically, the diameters obtained using AFM and SEM on dried solutions are significantly smaller than those determined via DLS, primarily because solvated particles have a larger diameter. Therefore, these diameter inconsistencies are expected. In short, none of these measurements is wrong; they are simply portraying the morphological properties using different techniques and conditions. Along with the hydrodynamic diameter, DLS also measures the polydispersity index (PDI), a measure of the heterogeneity of particle sizes in the mixture. PDI normally ranges from 0.0 to 1.0, and for perfectly uniform-sized nanoparticles, the PDI value would be 0.0, while a PDI value close to 1.0 indicates a highly polydisperse sample with multiple particle sizes; traditionally PDI values less than 0.5 are acceptable distributions in terms of size uniformity.[70] The PDI of EGaPs is 0.425 (Figure S3a) indicating satisfactory size uniformity.

The temporal stability of EGaPs for a period of 6 weeks was evaluated using DLS and displayed in Figure 2c,d. EGaPs were stored at a temperature of 4 °C for the 6-week experiment time period. The average diameter measured on day 0 (the day of preparation) was 182 nm and on day 42 was 194 nm. The size increased only about 7% after 6 weeks and there was no statistical difference ($p > 0.05$; One-way ANOVA with Tukey's multiple comparison test) showing remarkable stability of the particles. The distribution plots obtained from DLS measurements were overlapping on day 1 and day 42. The EGaPs also remained homogeneous over the same time frame judged by the nanoparticle suspension and their PDI values (Figure S3a,b). Furthermore, the ζ potential was measured to demonstrate the surface charge of the EGaPs. The ζ potentials of EGaIn-HA nanoparticles and EGaPs in PBS were 40.96 ± 1.06 and 50.90 ± 1.17 mV, respectively (Figure S3c). We performed additional measurements in DI water to investigate the effect of ions on PBS. The ζ potentials of EGaIn-HA and EGaPs in DI water were −93.67 ± 4.51 and −102.43 ± 4.44 mV, respectively (Figure S3b). The net increase in the ζ potential observed after the binding of BPD indicates the successful absorption of BPD onto the surface of EGaIn-HA. The carboxylic functionalized nanoparticles become positively charged due to the co-ion-specific effect of phosphate buffer.[71] Additionally, several studies have reported that cationic nanoparticles correlate with higher cellular uptake,[72−74] and hence, EGaPs aid in achieving the goal of increased cellular delivery of BPD.

Additionally, fluorescence spectroscopy was used to monitor the changes in fluorescence of BPD-bound EGaPs for long-term storage. Figure 2f shows the fluorescence spectra of EGaPs as a function of time for 6 weeks. The EGaPs when excited at 420 nm had an emission at 694 nm due to the presence of BPD.[75] The fluorescence of EGaPs was consistent over time with a minimal increase in intensity. The observation can be explained based on the fact that dequenched BPD has higher fluorescence emission. BPD is densely packed onto the EGaIn surface on day 1 (freshly prepared sample). Though not significant, there is a minimal release of BPD from our particles over the 42-day time period. This release of BPD reduces the number of BPD molecules on the nanoparticles leading to dequenching and therefore increase in the fluorescence signal of BPD. These fluorescence results coupled with the DLS analysis show that the EGaPs maintain constant diameter and consistent drug loading for up to 6 weeks when stored in a buffer solution at 4 °C.

3.2. Surface Characterization of EGaPs.

The energy-dispersive X-ray spectroscopy (EDS) map of the stable EGaPs obtained during the SEM measurements is shown in Figure S4. The EDS map clearly shows a uniform distribution of gallium and indium on the EGaP surface. However, it was not possible to distinguish the HA and BPD coating in the EDS map since the substrate was carbon tape and no contrast was observed. Thus, DRIFTS and Raman spectroscopy were used as more suitable techniques to gain additional insights into the ligands bound to the surface of the EGaPs. Both HA and BPD have carboxylic acid anchor groups that will react with the gallium oxide skin on the EGaIn nanoparticles to form surface carboxylates. The DRIFTS and Raman spectra shown in Figure S5 confirm the binding and show features representative of these surface carboxylates at ∼1600 cm^{-1} (ν_{as}) and ∼1300 cm^{-1} (ν_{s}).[76−78]

EGaPs had high light absorption, making UV−visible absorbance spectroscopy challenging to determine the concentration of BPD on the nanoparticle, as illustrated in Figure S1c. Thus, fluorescence measurements were used to quantify the concentration of BPD bound on the surface of EGaPs, with excitation at 420 nm and collecting emission at 694 nm.[79] A standard curve of the intensity of the fluorescence as a function of BPD concentration was used to estimate the loading efficiency on the EGaPs. The BPD loading efficiency was determined to be between 17 and 20% for EGaPs using our green synthesis method. To date, the loading efficiency on metallic nanoparticles is reported between 15 and 25% in most of the published work for targeted drug delivery.[46,80] For example, in one study, doxorubicin loading capacity was determined as 24% on EGaIn nanoparticles.[46] In another study, the loading efficiency of Ce6 (PS) on gold nanoparticles was reported as 18%.[80] These results indicate that the loading

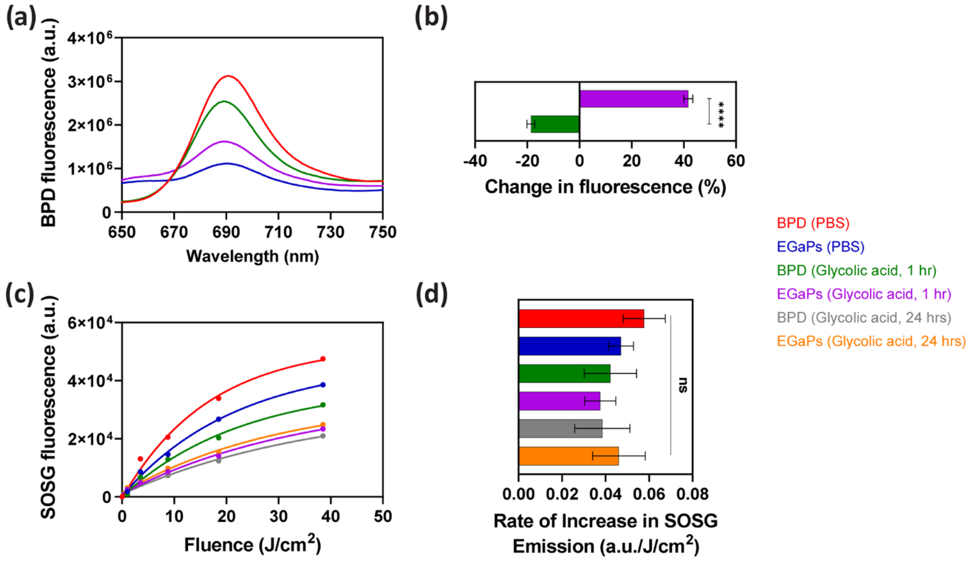

Figure 3. Photophysical and photochemical characterization of EGaPs. (a) Fluorescence spectra of BPD and EGaPs under physiologically relevant conditions. Fluorescence quenching was observed for EGaPs. (b) Change in fluorescence is defined as the fractional difference between maximum fluorescence emission intensity in PBS and maximum fluorescence emission intensity in glycolic acid. Photoactivity of EGaPs is improved in glycolic acid. (c) SOSG emission with the increasing fluence of the 690 nm wavelength of light irradiation. (d) Rate of increase in SOSG emission. The results are expressed as mean ± standard error with $n = 4$ separate experiments. (d): One-way ANOVA with Tukey's multiple comparison test: ns = $p > 0.05$.

efficiency of EGaPs is comparable to other metallic particles that are proposed for use in targeted cancer therapy.

3.3. BPD Release from EGaPs. One of the many benefits of employing nanoformulations in delivering drugs is that it allows for stimulus-triggered drug release to enhance delivery to target sites while minimizing adverse reactions in non-specific regions.[81,82] We hypothesize that since BPD is chemically adsorbed to the oxide layer and incubating EGaPs in physiologically relevant environments will release BPD from the oxide layer. To study the BPD release from EGaPs in a physiologically relevant environment, we performed several experiments in DI water and glycolic acid buffer solutions of varying pH (6, 7.4, and 9). We chose pH 6 buffer solution specifically since cancer cells are known to have mild acidic tumor microenvironments around this range.[83,84] We mimicked the tumor microenvironment for drug release studies by incubating EGaPs in pH 6 buffer solution at 37 °C. We also experimented with neutral (pH 7.4), basic (pH 9) buffer solutions and DI water as a control. The control DI water had constant BPD release between 11 and 15% at different time points of the experiment (Figure 2f). At the initial baseline time point of 0 h, all of the buffer solutions had ~1.5 to 2.5% BPD release. As the hours of incubation increased, the pH 9 had a steady release in BPD and peaked at 24 h with 69% of total BPD being released. This could be due to the reduction of gallium oxide to gallium ions by the basic buffer solution prompting the release of BPD.[68] On the other hand, pH 6 and 7.4 did not have significant BPD release till 6 h and had 32 and 26% drug release at 24 h, respectively. The amount of BPD released in pH 6 increased steadily thereafter and about 97% of total BPD was released at 96 h. Contrastingly, pH 7.4 peaked at 24 h and did not change at further time points. The release mechanism in pH 6 could be attributed to the disruption of the oxide layer leading to the fusion of EGaPs and ultimately release of BPD. Additionally, we performed DLS size analysis on the EGaIn-HA samples and found a significant increase in size after incubating in pH 6 buffer for 48 h (Table S1). The increase in size supports our reasoning and was in good agreement with the previously reported results.[46] Altogether we expect EGaPs to behave similarly under *in vivo* conditions due to the acidic tumor microenvironment and release BPD by fusion of EGaPs due to disruption of the oxide layer.

3.4. Photoactivity of EGaPs. One of the key motivations for conjugating BPD with EGaIn-HA is to improve the PS delivery and uptake in tumors. In addition, nanoformulation or nanoparticle association will improve the solubility in physiologically relevant buffers and help to retain BPD's photoactivity.[14] Hence, we evaluated the fluorescence emission spectra of free BPD and EGaPs in PBS and glycolic acid. From Figure 3a, we observe that the BPD fluorescence of EGaPs (blue line) is quenched in PBS as compared to the free BPD (red line). The reduction in the EGaP fluorescence is due to aggregation of many BPD molecules conjugated on the surface of EGaIn-HA. The proximity of BPD particles to each other and to the inorganic nanoparticle caused the fluorescence quenching. However, in the tumor microenvironment because of the slightly acidic pH of the cancer cytosol,[83,84] the oxide layer of EGaPs is degraded,[46,55] resulting in the release of BPD. We demonstrated the dequenching of EGaPs in glycolic acid buffer solution (pH 6), where the BPD fluorescence of EGaPs increased. Meanwhile, free BPD showed a reduction in the fluorescence emission in glycolic acid (pH 6) and this phenomenon has been observed for other types of PS and fluorescent dyes in acidic solutions.[85,86] This change in the fluorescence was further quantified in Figure 3b by calculating the fractional difference between maximum fluorescence emission intensity in PBS and maximum fluorescence emission intensity in glycolic acid. The fluorescence intensity of EGaPs significantly increased under biologically relevant conditions compared to free BPD.

BPD is predominantly a type II PS that primarily depends on oxygen in the environment to generate cytotoxic singlet oxygen molecules.[79] In this study, we explored the rate of singlet oxygen generation for both free BPD and EGaPs using a

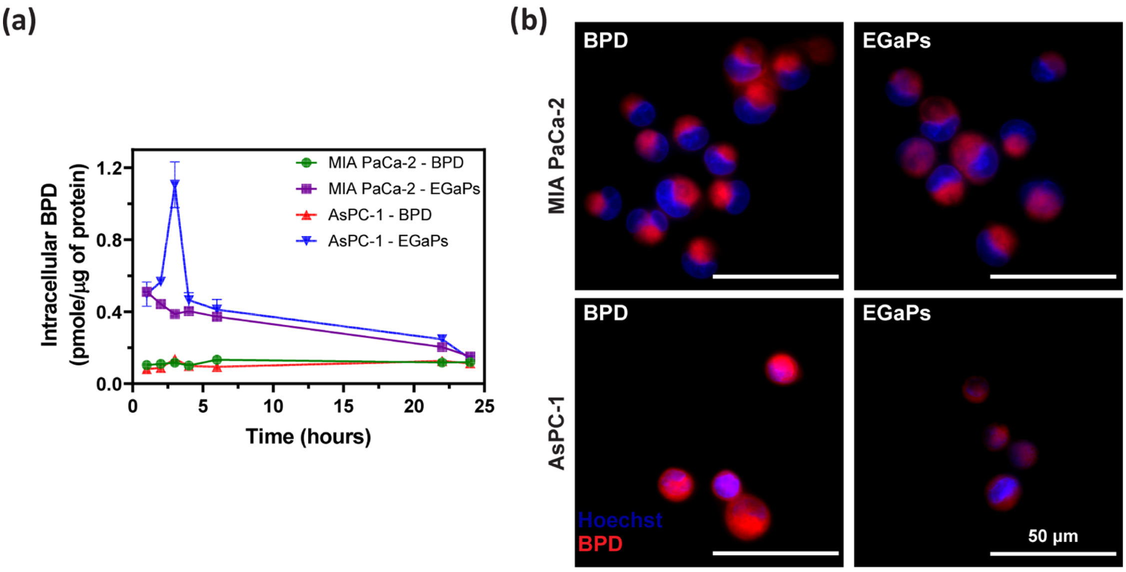

Figure 4. Cellular uptake of EGaPs and free BPD. (a) Quantification of intracellular BPD in MIA PaCa-2 and AsPC-1 cells incubated with EGaPs and free BPD using the extraction assay. (b) Live-cell fluorescence imaging shows the internalization of BPD in the cytosol of MIA PaCa-2 and AsPC-1 cells. Scale bar = 50 μm. The results are expressed as mean ± standard error with n = 3 separate experiments.

singlet oxygen-sensitive probe, SOSG. As SOSG is a cell-impermeable molecule, we performed the experiment *in vitro* using solutions. Upon irradiation with 690 nm light, SOSG fluorescence increased in a dose-dependent manner (Figure 3c). Free BPD produced higher singlet oxygen in PBS (red line) than EGaPs (blue line), and the lower singlet oxygen generation of EGaPs correlates with the fluorescence quenching shown in Figure 3a. Moreover, when the experiment was performed at a slightly lower pH (incubated with glycolic acid, pH of 6 for 1 or 24 h), the SOSG fluorescence intensity of both BPD and EGaPs reduced. This is due to the scavenging of singlet oxygen by the glycolic acid.[87−89] Furthermore, no differences in the rate of increase in SOSG fluorescence were observed for BPD and EGaPs in both PBS and glycolic acid (Figure 3d), suggesting that the global average of singlet oxygen production is unaffected by the pH of solution or presence of the nanoparticle.

Recent studies have shown the promising potential of liquid metal nanoparticles, such as EGaIn, as photothermal agents in both *in vitro* and *in vivo* models.[42,44,90] Following those studies, we investigated the thermal response of EGaPs when irradiated with a 690 nm wavelength of light. We observed a modest increase in the temperature of ∼5 °C from a baseline of 22 °C at the end of 30 min of irradiation at a power of 50 mW/cm^2 (Figure S6). However, a similar temperature rise (∼3.5 °C) was also seen in the control group (BPD only). This minimal temperature change is unlikely to cause photothermal-based cell killing. Typically, photothermal-mediated cell killing occurs when the local temperature reaches 43−45 °C or higher.[91,92] Studies that demonstrated the use of liquid metal nanoparticles for photothermal therapy of cancer have utilized a high power of 1 W (8 W/cm^2),[44] 1.8 W,[42] and 2 W/cm^2[90] to achieve maximum effectiveness. It is well known that PDT uses lower power than photothermal therapy. Here, we are achieving significant cell death with lower light doses due to the photodynamic action.

3.5. Quantification of EGaP Uptake in Pancreatic Cell Lines.

We investigated the uptake of EGaPs and free BPD in AsPC-1 and MIA PaCa-2 cells at different incubation time points using the extraction method to quantify the total BPD uptake. Extraction analysis (Figure 4a) showed variation in total BPD uptake between free BPD and EGaPs, as well as between AsPC-1 and MIA PaCa-2 cells. The total intracellular BPD concentration is reported in pmol/μg of protein. Both the cell lines had a greater amount of EGaP internalization at initial time points than free BPD. After 1 h of incubation, EGaPs had BPD uptakes of 0.51 ± 0.03 and 0.49 ± 0.12 pmol/μg of protein, whereas free BPD had an uptake of 0.08 ± 0.01 and 0.10 ± 0.01 for MIA PaCa-2 and AsPC-1, respectively. This may be due to the combined effort of both passive uptake via diffusion- and active receptor-mediated uptake as HA is known to target CD44 receptors.[20−22] Both the pancreatic cancer cell lines used in the study exhibit CD44 expression (Figure S7a), and the results were consistent with previous observations.[19] A competitive binding assay confirmed the targeting competence of EGaPs to the CD44 receptor due to HA coating. Any prior blocking of these receptors with free HA inhibited EGaP binding (Figure S7b). As the time of incubation is increased, the total amount of intracellular BPD for EGaPs reduced to 0.15 ± 0.02 and 0.14 ± 0.03 for MIA PaCa-2 and AsPC-1, respectively, whereas uptakes of free BPD increased to 0.12 ± 0.01 and 0.11 ± 0.01 for the same cell lines. This decrease in BPD for EGaPs may be due to intracellular BPD diffusing out of cells to reach equilibrium with the extracellular concentration. As BPD is known to fluoresce when activated with light, we performed live-cell fluorescence imaging to show the internalization of EGaPs compared to free BPD following 1 h of incubation. Figure 4b shows the internalization of BPD and EGaPs in the cytosol of MIA PaCa-2 and AsPC-1 cells, respectively. Free BPD exhibited slightly higher fluorescence than EGaPs at 1 h of incubation. This may be due to the higher amount of EGaPs internalized for both the cell lines resulting in the quenching of intracellular BPD, and this observation correlates with the extraction assay results in Figure 4a.

3.6. In Vitro Photodestruction of Pancreatic Cells with Light-Activated EGaPs.

Before examining the phototoxicity of EGaPs, we assessed the associated toxicity of HA and EGaIn-HA in AsPC-1 cells. HA had almost no toxicity

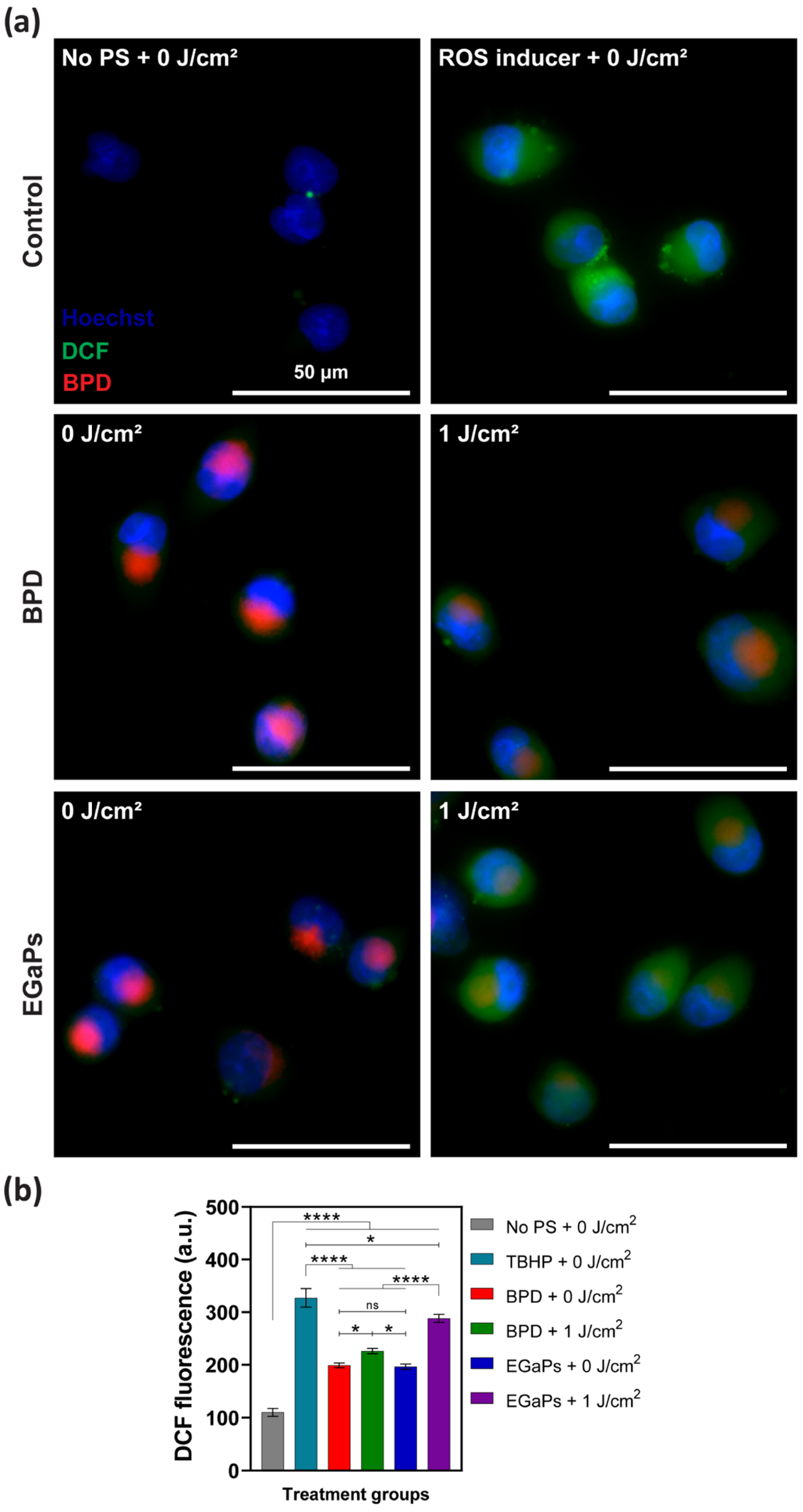

Figure 5. Intracellular ROS analysis in MIA PaCa-2 cells with the DCFDA assay. (a) Fluorescence images of MIA PaCa-2 live cells treated with no PS, 200 μM tert-butyl hydroperoxide (ROS inducer), BPD, and EGaPs with 0 and 1 J/cm^2. Scale bar = 50 μm. DCF signal (ROS) is pseudo-colored in green, BPD in red, and nuclear staining (Hoechst) in blue. (b) Quantification of DCF fluorescence intensity per cell. EGaPs produced significantly higher ROS after PDT when compared to free BPD. The results are expressed as mean ± standard error (n = 30 images across three separate experiments) and analyzed using one-way ANOVA with Tukey's multiple comparison test. ns = $p > 0.05$, * = $p < 0.05$, and **** = $p < 0.0001$.

until the concentration of 10 μg/mL for 1 and 24 h of incubation, while an increase in the viability was observed when HA was incubated with cells for 48 h (Figure S8a). This increase in cell viability was expected for HA with 48 h of incubation as it is known to enhance cellular proliferation and viability.[93,94] When the cells were incubated with 100 μg/mL HA for 24 h, we observed ∼10% toxicity, while when incubated for 1 or 48 h had none. At a higher concentration

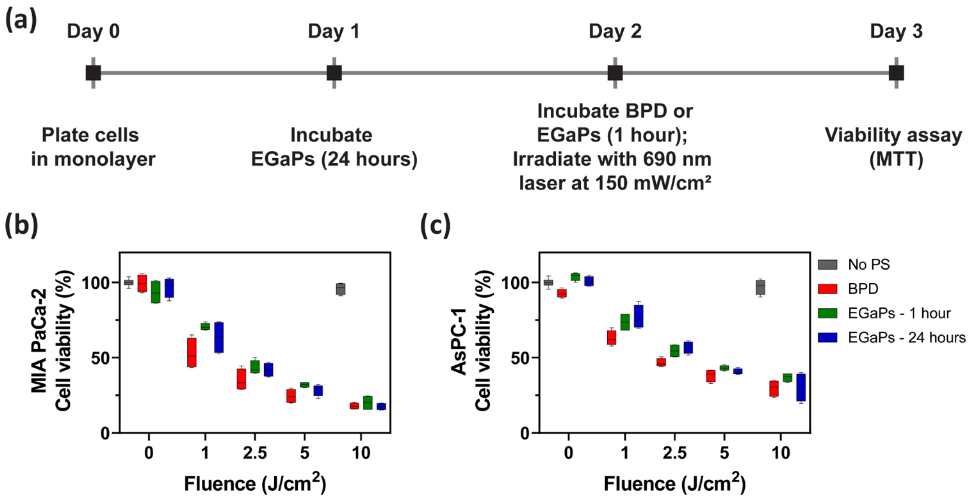

Figure 6. Photodestruction of pancreatic cells with light-activated EGaPs. (a) Schematic of the experimental timeline for PDT with EGaPs and free BPD. Dose response killing of light-activated EGaPs and free BPD in (b) MIA PaCa-2 and (c) AsPC-1 cells (n = 4 separate experiments).

of 750 μg/mL, we observed ∼12 to 20% toxicity for all of the incubation time points. Based on the results of this experiment, we decided to coat EGaIn with 0.1 mg/mL HA. Next, we investigated the dark toxicity of EGaIn coated with 0.1 mg/mL HA. The concentration of EGaIn-HA was increased to 160 μg/mL and incubated at three different time points of incubation: 1, 24, and 48 h. EGaIn-HA did not have any significant effect on the viability of the cells and a modest toxicity of ∼3 to 7% was observed (Figure S8b). This result shows that the liquid metal nanoparticles are nontoxic and are biocompatible at the concentrations used in this study. Throughout our experiments, the concentrations of EGaIn in EGaPs incubated with cells were <100 μg/mL.

Next, we investigated the cellular ROS generation potential of EGaPs as it determines the anticancer activity. Live-cell fluorescence imaging showed enhanced DCF fluorescence (pseudo-colored in green), implying high intracellular ROS after induction with TBHP and PDT with EGaPs and free BPD (Figure 5a). DCF fluorescence per cell was quantified and is shown in Figure 5b. Altogether TBHP, EGaPs, and free BPD with and without light irradiation induced a significant quantity of ROS when compared to the control. EGaPs had 46% higher ROS generation upon light activation, while free BPD had a 13% hike in ROS population when compared to their respective no-light conditions. EGaPs induced a similar level of ROS as free BPD under no-light conditions but had significantly higher 1.27-fold ROS generation upon irradiation.

Finally, we assessed the phototoxicity of EGaPs and free BPD in MIA PaCa-2 and AsPC-1 cells. Cells were incubated with EGaPs for 1 or 24 h, while free BPD was incubated for 1 h at a concentration of 0.25 μM of BPD equivalent (EGaIn concentration in dilution was ∼40 μg/mL). The experimental detail for PDT is illustrated in Figure 6a. At 24 h after irradiation, viability was assessed using the MTT assay. Free BPD and EGaPs had negligible toxicity under no-light conditions but when activated showed a light dose-responsive cell killing in both MIA PaCa-2 and AsPC-1 cells (Figure 6b,c respectively). These results were expected and matched previously published reports on these cell lines.[95−97] A significant difference in phototoxicity was observed for EGaPs incubated for 1 or 24 h versus free BPD at 1 J/cm^2 (Tables S2 and S3), while no significance was observed at higher light doses. Overall, total cell killing was higher in MIA PaCa-2 than in AsPC-1 cells. Although the total amount of BPD from EGaPs internalized at 1 h of incubation (∼0.5 pmol/μg of protein) was significantly higher than at 24 h (∼0.14 pmol/μg of protein), the BPD internalized at 24 h is enough to achieve effective results. Besides, the total BPD internalized from incubating free BPD at 1 h was ∼0.08 pmol/μg of protein, which suggests that we could have achieved similar PDT efficacy with EGaPs at an even lower concentration than 0.25 μM of BPD equivalent that was used. Furthermore, free BPD being hydrophobic requires organic solvent such as DMSO to dissolve to be used for any *in vitro* studies. The presence of these organic solvents can result in cellular toxicity. As a result, they cannot be used in patients (*in vivo*) by themselves and need a nanocarrier or lipid-based nanoformulations. EGaP is a nanoformulation we developed to aid in the delivery of BPD for PDT. As EGaPs had better overall results than free BPD due to their greater BPD uptake at an initial time point, higher ROS generation, and CD44 receptor targeting competency, we anticipate EGaPs to be better PDT agents than free BPD.

3.7. In Vivo Photodynamic Efficacy of EGaPs.

After the *in vitro* PDT experiments with EGaPs, we evaluated their efficacy in treating the AsPC-1 pancreatic cancer tumors established in nude mice. The mice (each group contained four mice) were randomly divided into three groups: no-treatment, EGaPs with laser, and liposomal BPD with laser. Liposomes are generally used as BPD delivery agents and have been previously used in *in vivo* PDT studies.[13,98] Here, we compared the efficacy of liposomal BPD to that of EGaPs *in vivo*. The weight of the mice was recorded along with the tumor volume for 30 days after PDT. Figure 7a shows the normalized tumor volume of each group. As expected, the tumor volume of the nontreated group increased over time, while tumors treated with EGaPs and liposomal BPD responded to PDT and had a reduction in the tumor volume. A minimal loss in weight was observed on day 2 after PDT (∼8%) for both liposomal BPD- and EGaP-treated groups (Figure 7b). Thereafter, the body weight increased and showed no statistical difference from the no-treatment group. Additionally, pictures of representative tumors from each treatment group are shown in Figure 7c. Liposomal BPD- and EGaP-treated tumors developed swelling

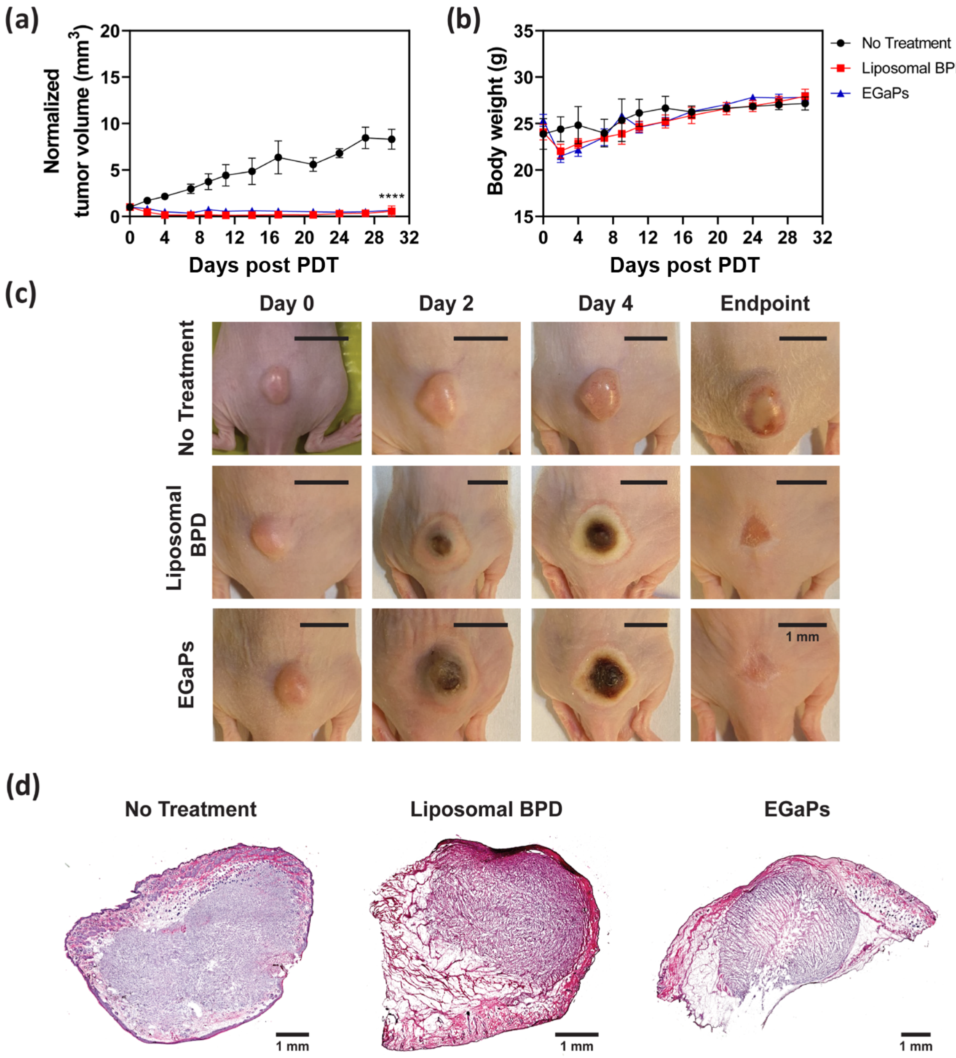

Figure 7. *In vivo* treatment efficacy of EGaPs in the AsPC-1 tumor model. (a) Normalized tumor volume of mice treated with EGaPs and traditionally used liposomal formulation of BPD. (b) Changes in the weight of the mice after PDT over duration of the experiment. The values reported are mean ± standard error. (c) Photographs of the representative tumor from each treatment group on varying days after PDT. (d) H&E image of the tumor from each treatment group. Scale bar = 1 mm. The results are expressed as mean ± standard error. (a): Two-way ANOVA with Tukey's multiple comparison test. **** = $p < 0.0001$.

and scarring on day 2 as expected. A higher degree of scarring was noticed on day 4. As the days progressed, the tumor volume did not increase and continued to reduce. The tumors in both the treated groups were significantly different from the no-treatment group at the endpoint of the experiment (day 30) (Figure 7c).

Finally, we probed the therapeutic effects of EGaP PDT in the tumors 2 days after treatment via histological analysis. Figure 7d shows the H&E image of the representative tumor from each treatment group. Tumors from the no-treatment group had less necrotic regions when compared to the liposomal BPD or EGaP-treated tumors. Moreover, we quantified the percent necrotic volume imparted in the tumor by each treatment with a custom-written MATLAB algorithm to calculate the total necrotic area within the tumor (Figure S9).[99,100] The nontreated tumors had ∼10% necrotic area, while liposomal BPD-based PDT caused 1.7-times more necrosis. On the other hand, EGaP PDT significantly caused 2.3-times higher necrosis in the tumor than the no-treatment. The goal of this study was to characterize the novel liquid metal nanoparticles for delivering PS for PDT. The *in vivo* PDT efficacy of thus prepared EGaPs was compared to liposomal BPD formulations that are more widely used in the field.[13,98] In our study, liposomal BPD and EGaPs had similar tumor inhibitory effects, indicating that BPD's cytotoxic effect was not compromised when delivered via EGaPs. Furthermore, we believe that EGaPs have greater leverage owing to higher ROS generation, their competence for targeting CD44 receptors, and pH-triggered drug release. In addition, EGaPs can also be used as a photoacoustic imaging contrast agent due to their high light absorption property, an area that will be explored in future studies. In summary, the results from our study suggest that EGaPs can serve as a versatile agent for targeted drug delivery, specifically for PDT, leading to efficient antitumor effects.

4. CONCLUSIONS

In this study, a new liquid metal-based PDT drug delivery platform has been developed for cancer treatment. We formulated EGaIn nanoparticles coated with a water-soluble targeting ligand, HA, and a PDT agent, BPD, forming EGaPs via a facile ultrasonication method. The fabrication process is green, very straightforward, and timesaving compared to the complex procedures for another inorganic such as gold-based nanoparticles. The spherical EGaPs formed a highly biocompatible nanoplatform with suitable particle size and positive charge, which facilitate the cell uptake for the nanoparticles. We explored the binding mechanism of HA and BPD on EGaIn using vibrational and fluorescence measurements. Acid-triggered release of BPD from these nanoparticles showed the capability of releasing PS at the targeted site without external energy due to their inherent pH-sensitive properties. Fluorescence imaging confirmed the uptake of BPD from EGaPs and targeting capability. Systematic investigation of phototoxicity experiment *in vitro* confirmed that EGaPs generate intracellular ROS and damage cancer cells under NIR radiation. *In vivo* xenograft treatment studies showed that EGaP administration can cause tumor regression with tangible therapeutic effect. The outcome reveals that EGaPs provide a promising vehicle for liquid metal nanoparticle-based drug delivery systems, contributing to the development of synergistic and complementary strategies for cancer therapy.

■ ASSOCIATED CONTENT

Supporting Information

The Supporting Information is available free of charge at https://pubs.acs.org/doi/10.1021/acsanm.1c04353.

> Photographs of EGaIn-HA and EGaPs with their absorption spectra (Figure S1); AFM image of EGaPs with size distribution (Figure S2); polydispersity index, ζ potential, and photograph of suspension of EGaPs (Figure S3); SEM image of EGaPs with EDS elemental analysis (Figure S4). DRIFTS and Raman spectra of EGaIn-HA and EGaPs (Figure S5); photothermal response of EGaPs, EGaIn-HA, and free BPD when irradiated at 690 nm laser (Figure S6); CD44 expression of MIA PaCa-2 and AsPC-1 cells and CD44 targeting competency of EGaPs (Figure S7). Cytotoxicity of HA and EGaIn-HA in AsPC-1 cells (Figure S8); quantification of necrotic regions in the tumor after EGaPs or liposomal BPD-based PDT treatments (Figure S9). DLS size measurements of EGaIn-HA after incubating in pH 6 buffer solution (Table S1). ANOVA analysis of phototoxicity of EGaPs incubated for 1 or 24 h with free BPD in MIA PaCa-2 (Table S2) and AsPC-1 (Table S3) cells (PDF)

■ AUTHOR INFORMATION

Corresponding Authors

Michelle Foster − *Department of Chemistry, University of Massachusetts Boston, Boston, Massachusetts 02125, United States;* orcid.org/0000-0002-5051-2878; Email: michelle.foster@umb.edu

Srivalleesha Mallidi − *Department of Biomedical Engineering, Tufts University, Medford, Massachusetts 02155, United States;* orcid.org/0000-0003-1547-1764; Email: srivalleesha.mallidi@tufts.edu

Authors

Sabrina S. Hafiz − *Department of Chemistry, University of Massachusetts Boston, Boston, Massachusetts 02125, United States*

Marvin Xavierselvan − *Department of Biomedical Engineering, Tufts University, Medford, Massachusetts 02155, United States*

Sumeyra Gokalp − *Department of Chemistry, University of Massachusetts Boston, Boston, Massachusetts 02125, United States*

Daniela Labadini − *Department of Chemistry, University of Massachusetts Boston, Boston, Massachusetts 02125, United States*

Sebastian Barros − *Department of Chemistry, University of Massachusetts Boston, Boston, Massachusetts 02125, United States*

Jeanne Duong − *Department of Biomedical Engineering, Tufts University, Medford, Massachusetts 02155, United States*

Complete contact information is available at: https://pubs.acs.org/10.1021/acsanm.1c04353

Author Contributions

§S.S.H., M.X., and S.G. shared co-first authors and contributed equally to this work.

Funding

The authors gratefully acknowledge funds from the National Institute of Health grant U54CA156732 (subaward to Foster and Mallidi) and R21CA263694 (Mallidi).

Notes

The authors declare no competing financial interest.

■ ACKNOWLEDGMENTS

The authors thank Dr. Ljubica Petrovic for assisting with *in vitro* experiments. They would also like to thank Genevieve M. Asselin for her assistance in collecting SEM images of EGaPs.

■ REFERENCES

(1) Siegel, R. L.; Miller, K. D.; Fuchs, H. E.; Jemal, A. Cancer Statistics, 2021. *CA-Cancer J. Clin.* **2021**, *71*, 7−33.

(2) Hidalgo, M. Pancreatic Cancer. *N. Engl. J. Med.* **2010**, *362*, 1605−1617.

(3) Gamboa, A. C.; Lee, R. M.; Maithel, S. K. The role of radiation for pancreatic adenocarcinoma. *J. Pancreatol.* **2020**, *3*, 72−80.

(4) Li, J.; Wientjes, M. G.; Au, J. L. S. Pancreatic cancer: pathobiology, treatment options, and drug delivery. *AAPS J.* **2010**, *12*, 223−232.

(5) Bown, S. G.; Rogowska, A. Z.; Whitelaw, D. E.; Lees, W. R.; Lovat, L. B.; Ripley, P.; Jones, L.; Wyld, P.; Gillams, A.; Hatfield, A. W. R. Photodynamic therapy for cancer of the pancreas. *Gut* **2002**, *50*, 549−557.

(6) Jermyn, M.; Davis, S. C.; Dehghani, H.; Huggett, M. T.; Hasan, T.; Pereira, S. P.; Bown, S. G.; Pogue, B. W. CT contrast predicts pancreatic cancer treatment response to verteporfin-based photodynamic therapy. *Phys. Med. Biol.* **2014**, *59*, 1911−1921.

(7) Huggett, M. T.; Jermyn, M.; Gillams, A.; Illing, R.; Mosse, S.; Novelli, M.; Kent, E.; Bown, S. G.; Hasan, T.; Pogue, B. W.; Pereira, S. P. Phase I/II study of verteporfin photodynamic therapy in locally advanced pancreatic cancer. *Br. J. Cancer* **2014**, *110*, 1698−1704.

(8) Henderson, B. W.; Dougherty, T. J. How does photodynamic therapy work? *Photochem. Photobiol.* **1992**, *55* (), 145−157 DOI: 10.1111/j.1751-1097.1992.tb04222.x.

(9) Lucky, S. S.; Soo, K. C.; Zhang, Y. Nanoparticles in Photodynamic Therapy. *Chem. Rev.* **2015**, *115*, 1990−2042.

(10) Wilson, B. C.; Patterson, M. S.; Lilge, L. Implicit and explicit dosimetry in photodynamic therapy: a New paradigm. *Lasers Med. Sci.* **1997**, *12*, 182−199.

(11) Spring, B. Q.; Bryan Sears, R.; Zheng, L. Z.; Mai, Z.; Watanabe, R.; Sherwood, M. E.; Schoenfeld, D. A.; Pogue, B. W.; Pereira, S. P.; Villa, E.; Hasan, T. A photoactivable multi-inhibitor nanoliposome for

tumour control and simultaneous inhibition of treatment escape pathways. *Nat. Nanotechnol.* **2016**, *11*, 378−387.

(12) Hu, H.; Feng, W.; Qian, X.; Yu, L.; Chen, Y.; Li, Y. Emerging Nanomedicine-Enabled/Enhanced Nanodynamic Therapies beyond Traditional Photodynamics. *Adv. Mater.* **2021**, *33*, 2005062.

(13) Huang, H. C.; Mallidi, S.; Liu, J.; Chiang, C. T.; Mai, Z.; Goldschmidt, R.; Ebrahim-Zadeh, N.; Rizvi, I.; Hasan, T. Photodynamic Therapy Synergizes with Irinotecan to Overcome Compensatory Mechanisms and Improve Treatment Outcomes in Pancreatic Cancer. *Cancer Res.* **2016**, *76*, 1066−1077.

(14) Obaid, G.; Jin, W.; Bano, S.; Kessel, D.; Hasan, T. Nanolipid Formulations of Benzoporphyrin Derivative: Exploring the Dependence of Nanoconstruct Photophysics and Photochemistry on Their Therapeutic Index in Ovarian Cancer Cells. *Photochem. Photobiol.* **2019**, *95*, 364−377.

(15) Kiesslich, T.; Berlanda, J.; Plaetzer, K.; Krammer, B.; Berr, F. Comparative characterization of the efficiency and cellular pharmacokinetics of Foscan- and Foslip-based photodynamic treatment in human biliary tract cancer cell lines. *Photochem. Photobiol. Sci.* **2007**, *6*, 619−627.

(16) Lassalle, H.-P.; Dumas, D.; Gräfe, S.; D'Hallewin, M.-A.; Guillemin, F.; Bezdetnaya, L. Correlation between in vivo pharmacokinetics, intratumoral distribution and photodynamic efficiency of liposomal mTHPC. *J. Controlled Release* **2009**, *134*, 118−124.

(17) Sebak, A. A.; Gomaa, I. E. O.; ElMeshad, A. N.; AbdelKader, M. H. Targeted photodynamic-induced singlet oxygen production by peptide-conjugated biodegradable nanoparticles for treatment of skin melanoma. *Photodiagn. Photodyn. Ther.* **2018**, *23*, 181−189.

(18) Ringel, J.; Jesnowski, R.; Schmidt, C.; Ringel, J.; Köhler, H. J.; Rychly, J.; Batra, S. K.; Löhr, M. CD44 in normal human pancreas and pancreatic carcinoma cell lines. *Teratog., Carcinog., Mutagen.* **2001**, *21*, 97−106.

(19) Wei, H.-J.; Yin, T.; Zhu, Z.; Shi, P.-F.; Tian, Y.; Wang, C.-Y. Expression of CD44, CD24 and ESA in pancreatic adenocarcinoma cell lines varies with local microenvironment. *Hepatobiliary Pancreatic Dis. Int.* **2011**, *10*, 428−434.

(20) Spadea, A.; Rios de la Rosa, J. M.; Tirella, A.; Ashford, M. B.; Williams, K. J.; Stratford, I. J.; Tirelli, N.; Mehibel, M. Evaluating the Efficiency of Hyaluronic Acid for Tumor Targeting via CD44. *Mol. Pharmaceutics* **2019**, *16*, 2481−2493.

(21) Misra, S.; Hascall, V. C.; Markwald, R. R.; Ghatak, S. Interactions between hyaluronan and its receptors (CD44, RHAMM) regulate the activities of inflammation and cancer. *Front. Immunol.* **2015**, *6*, 201.

(22) Platt, V. M.; Szoka, F. C. Anticancer Therapeutics: Targeting Macromolecules and Nanocarriers to Hyaluronan or CD44, a Hyaluronan Receptor. *Mol. Pharmaceutics* **2008**, *5*, 474−486.

(23) Yan, Y.; Zuo, X.; Wei, D. Concise Review: Emerging Role of CD44 in Cancer Stem Cells: A Promising Biomarker and Therapeutic Target. *Stem Cells Transl. Med.* **2015**, *4*, 1033−1043.

(24) García Calavia, P.; Bruce, G.; Pérez-García, L.; Russell, D. A. Photosensitiser-gold nanoparticle conjugates for photodynamic therapy of cancer. *Photochem. Photobiol. Sci.* **2018**, *17*, 1534−1552.

(25) Yi, G.; Hong, S. H.; Son, J.; Yoo, J.; Park, C.; Choi, Y.; Koo, H. Recent advances in nanoparticle carriers for photodynamic therapy. *Quant Imaging Med. Surg.* **2018**, *8*, 433−443.

(26) Shang, L.; Zhou, X.; Zhang, J.; Shi, Y.; Zhong, L. Metal Nanoparticles for Photodynamic Therapy: A Potential Treatment for Breast Cancer. *Molecules* **2021**, *26*, No. 6532.

(27) Mao, C.; Xiang, Y.; Liu, X.; Cui, Z.; Yang, X.; Li, Z.; Zhu, S.; Zheng, Y.; Yeung, K. W. K.; Wu, S. Repeatable Photodynamic Therapy with Triggered Signaling Pathways of Fibroblast Cell Proliferation and Differentiation To Promote Bacteria-Accompanied Wound Healing. *ACS Nano* **2018**, *12*, 1747−1759.

(28) Jia, X.; Ahmad, I.; Yang, R.; Wang, C. Versatile graphene-based photothermal nanocomposites for effectively capturing and killing bacteria, and for destroying bacterial biofilms. *J. Mater. Chem. B* **2017**, *5*, 2459−2467.

(29) Lei, W.; Ren, K.; Chen, T.; Chen, X.; Li, B.; Chang, H.; Ji, J. Polydopamine Nanocoating for Effective Photothermal Killing of Bacteria and Fungus upon Near-Infrared Irradiation. *Adv. Mater. Interfaces* **2016**, *3*, No. 1600767.

(30) Liu, X. Y.; Wang, J. Q.; Ashby, C. R., Jr.; Zeng, L.; Fan, Y. F.; Chen, Z. S. Gold nanoparticles: synthesis, physiochemical properties and therapeutic applications in cancer. *Drug Discovery Today* **2021**, *26*, 1284−1292.

(31) Penon, O.; Marin, M. J.; Russell, D. A.; Perez-Garcia, L. Water soluble, multifunctional antibody-porphyrin gold nanoparticles for targeted photodynamic therapy. *J. Colloid Interface Sci.* **2017**, *496*, 100−110.

(32) Kim, H. S.; Lee, D. Y. Near-Infrared-Responsive Cancer Photothermal and Photodynamic Therapy Using Gold Nanoparticles. *Polymers* **2018**, *10*, No. 961.

(33) He, J. S.; Liu, S. J.; Zhang, Y. R.; Chu, X. D.; Lin, Z. B.; Zhao, Z.; Qiu, S. H.; Guo, Y. G.; Ding, H.; Pan, Y. L.; Pan, J. h. The Application of and Strategy for Gold Nanoparticles in Cancer Immunotherapy. *Front. Pharmacol.* **2021**, *12*, No. 687399.

(34) Mao, C.; Xiang, Y.; Liu, X.; Cui, Z.; Yang, X.; Yeung, K. W. K.; Pan, H.; Wang, X.; Chu, P. K.; Wu, S. Photo-Inspired Antibacterial Activity and Wound Healing Acceleration by Hydrogel Embedded with Ag/Ag@AgCl/ZnO Nanostructures. *ACS Nano* **2017**, *11*, 9010−9021.

(35) Xiang, Y.; Zhou, Q.; Li, Z.; Cui, Z.; Liu, X.; Liang, Y.; Zhu, S.; Zheng, Y.; Yeung, K. W. K.; Wu, S. A Z-scheme heterojunction of ZnO/CDots/C3N4 for strengthened photoresponsive bacteria-killing and acceleration of wound healing. *J. Mater. Sci. Technol.* **2020**, *57*, 1−11.

(36) Mesquita, M. Q.; Dias, C. J.; Gamelas, S.; Fardilha, M.; Neves, M. G. P. M. S.; Faustino, M. A. F. An insight on the role of photosensitizer nanocarriers for Photodynamic Therapy. *Anais da Academia Brasileira de Ciências* **2018**, *90*, 1101−1130.

(37) Pasparakis, G. Light-Induced Generation of Singlet Oxygen by Naked Gold Nanoparticles and its Implications to Cancer Cell Phototherapy. *Small* **2013**, *9*, 4130−4134.

(38) Hainfeld, J. F.; O'Connor, M. J.; Lin, P.; Qian, L.; Slatkin, D. N.; Smilowitz, H. M. Infrared-transparent gold nanoparticles converted by tumors to infrared absorbers cure tumors in mice by photothermal therapy. *PLoS One* **2014**, *9*, e88414.

(39) Xie, W.; Allioux, F. M.; Ou, J. Z.; Miyako, E.; Tang, S. Y.; Kalantar-Zadeh, K. Gallium-Based Liquid Metal Particles for Therapeutics. *Trends Biotechnol.* **2021**, *39*, 624−640.

(40) Kim, D.; Hwang, J.; Choi, Y.; Kwon, Y.; Jang, J.; Yoon, S.; Choi, J. Effective delivery of anti-cancer drug molecules with shape transforming liquid metal particles. *Cancers* **2019**, *11*, No. 1666.

(41) Dickey, M. D.; Chiechi, R. C.; Larsen, R. J.; Weiss, E. A.; Weitz, D. A.; Whitesides, G. M. Eutectic Gallium-Indium (EGaIn): A Liquid Metal Alloy for the Formation of Stable Structures in Microchannels at Room Temperature. *Adv. Funct. Mater.* **2008**, *18*, 1097−1104.

(42) Xia, N.; Li, N.; Rao, W.; Yu, J.; Wu, Q.; Tan, L.; Li, H.; Gou, L.; Liang, P.; Li, L.; Meng, X. Multifunctional and flexible ZrO2-coated EGaIn nanoparticles for photothermal therapy. *Nanoscale* **2019**, *11*, 10183−10189.

(43) Lu, Y.; Lin, Y.; Chen, Z.; Hu, Q.; Liu, Y.; Yu, S.; Gao, W.; Dickey, M. D.; Gu, Z. Enhanced Endosomal Escape by Light-Fueled Liquid-Metal Transformer. *Nano Lett.* **2017**, *17*, 2138−2145.

(44) Chechetka, S. A.; Yu, Y.; Zhen, X.; Pramanik, M.; Pu, K.; Miyako, E. Light-driven liquid metal nanotransformers for biomedical theranostics. *Nat. Commun.* **2017**, *8*, No. 15432.

(45) Kim, J.-H.; Kim, S.; So, J.-H.; Kim, K.; Koo, H.-J. Cytotoxicity of Gallium−Indium Liquid Metal in an Aqueous Environment. *ACS Appl. Mater. Interfaces* **2018**, *10*, 17448−17454.

(46) Lu, Y.; Hu, Q.; Lin, Y.; Pacardo, D. B.; Wang, C.; Sun, W.; Ligler, F. S.; Dickey, M. D.; Gu, Z. Transformable liquid-metal nanomedicine. *Nat. Commun.* **2015**, *6*, No. 10066.

(47) Collery, P.; Keppler, B.; Madoulet, C.; Desoize, B. Gallium in cancer treatment. *Crit. Rev. Oncol. Hematol.* **2002**, *42*, 283−296.

(48) Wu, Q.; Xia, N.; Long, D.; Tan, L.; Rao, W.; Yu, J.; Fu, C.; Ren, X.; Li, H.; Gou, L.; et al. Dual-Functional Supernanoparticles with Microwave Dynamic Therapy and Microwave Thermal Therapy. *Nano Lett.* **2019**, *19*, 5277−5286.

(49) He, J.; Shi, F.; Wu, J.; Ye, J. Shape Transformation Mechanism of Gallium−Indium Alloyed Liquid Metal Nanoparticles. *Adv. Mater. Interfaces* **2021**, *8*, No. 2001874.

(50) Wang, D.; Wu, Q.; Guo, R.; Lu, C.; Niu, M.; Rao, W. Magnetic liquid metal loaded nano-in-micro spheres as fully flexible theranostic agents for SMART embolization. *Nanoscale* **2021**, *13*, 8817−8836.

(51) Day, J. A.; Cohen, S. M. Investigating the Selectivity of Metalloenzyme Inhibitors. *J. Med. Chem.* **2013**, *56*, 7997−8007.

(52) Hafiz, S. S.; Labadini, D.; Riddell, R.; Wolff, E. P.; Xavierselvan, M.; Huttunen, P. K.; Mallidi, S.; Foster, M. Surfaces and Interfaces of Liquid Metal Core−Shell Nanoparticles under the Microscope. *Part. Part. Syst. Charact.* **2020**, *37*, 1900469.

(53) Tevis, I. D.; Newcomb, L. B.; Thuo, M. Synthesis of Liquid Core−Shell Particles and Solid Patchy Multicomponent Particles by Shearing Liquids Into Complex Particles (SLICE). *Langmuir* **2014**, *30*, 14308−14313.

(54) Vasi, A.-M.; Popa, M. I.; Butnaru, M.; Dodi, G.; Verestiuc, L. Chemical functionalization of hyaluronic acid for drug delivery applications. *Mater. Sci. Eng.: C* **2014**, *38*, 177−185.

(55) Yamaguchi, A.; Mashima, Y.; Iyoda, T. Reversible Size Control of Liquid-Metal Nanoparticles under Ultrasonication. *Angew. Chem., Int. Ed.* **2015**, *54*, 12809−12813.

(56) Demiral, A.; Verimli, N.; Goralı, S. İ.; Yılmaz, H.; Çulha, M.; Erdem, S. S. A Rational design of multi-functional nanoplatform: Fluorescent-based "off-on" theranostic gold nanoparticles modified with D-α-Tocopherol succinate. *J. Photochem. Photobiol., B* **2021**, *222*, 112261.

(57) Gan, T.; Shang, W.; Handschuh-Wang, S.; Zhou, X. Light-Induced Shape Morphing of Liquid Metal Nanodroplets Enabled by Polydopamine Coating. *Small* **2019**, *15*, No. 1804838.

(58) Ernsting, M. J.; Murakami, M.; Roy, A.; Li, S.-D. Factors controlling the pharmacokinetics, biodistribution and intratumoral penetration of nanoparticles. *J. Controlled Release* **2013**, *172*, 782−794.

(59) Wu, W.; Luo, L.; Wang, Y.; Wu, Q.; Dai, H.-B.; Li, J.-S.; Durkan, C.; Wang, N.; Wang, G.-X. Endogenous pH-responsive nanoparticles with programmable size changes for targeted tumor therapy and imaging applications. *Theranostics* **2018**, *8*, 3038−3058.

(60) Bhatia, S. Nanoparticles Types, Classification, Characterization, Fabrication Methods and Drug Delivery Applications. In *Natural Polymer Drug Delivery Systems*, Bhatia, S., Ed.; Springer International Publishing, 2016; pp. 33−93.

(61) Longmire, M.; Choyke, P. L.; Kobayashi, H. Clearance properties of nano-sized particles and molecules as imaging agents: considerations and caveats. *Nanomedicine (Lond)* **2008**, *3*, 703−717.

(62) Yetisgin, A. A.; Cetinel, S.; Zuvin, M.; Kosar, A.; Kutlu, O. Therapeutic Nanoparticles and Their Targeted Delivery Applications. *Molecules* **2020**, *25*, No. 2193.

(63) Whitesides, G. M. The 'right' size in nanobiotechnology. *Nat. Biotechnol.* **2003**, *21*, 1161−1165.

(64) Peer, D.; Karp, J. M.; Hong, S.; Farokhzad, O. C.; Margalit, R.; Langer, R. Nanocarriers as an emerging platform for cancer therapy. *Nat. Nanotechnol.* **2007**, *2*, 751−760.

(65) Delvallée, A.; Feltin, N.; Ducourtieux, S.; Trabelsi, M.; Hochepied, J. F., *Comparison of nanoparticle diameter measurements by Atomic Force Microscopy and Scanning Electron Microscopy*, International Congress of Metrology, 2013.

(66) Gokalp, S.; Horton, W.; Jónsdóttir-Lewis, E. B.; Foster, M.; Török, M. Laboratory exercise for studying the morphology of heat-denatured and amyloid aggregates of lysozyme by atomic force microscopy. *Biochem. Mol. Biol. Educ.* **2018**, *46*, 162−171.

(67) Eaton, P.; Quaresma, P.; Soares, C.; Neves, C.; de Almeida, M. P.; Pereira, E.; West, P. A direct comparison of experimental methods to measure dimensions of synthetic nanoparticles. *Ultramicroscopy* **2017**, *182*, 179−190.

(68) Kim, J. H.; Park, Y. J.; Kim, S.; So, J. H.; Koo, H. J. Effect of Surrounding Solvents on Interfacial Behavior of Gallium-Based Liquid Metal Droplets. *Materials* **2022**, *15*, No. 706.

(69) Carvalho, P. M.; Felicio, M. R.; Santos, N. C.; Goncalves, S.; Domingues, M. M. Application of Light Scattering Techniques to Nanoparticle Characterization and Development. *Front. Chem.* **2018**, *6*, No. 237.

(70) Anselmo, A. C.; Mitragotri, S. Impact of particle elasticity on particle-based drug delivery systems. *Adv. Drug Delivery Rev.* **2017**, *108*, 51−67.

(71) Cugia, F.; Monduzzi, M.; Ninham, B. W.; Salis, A. Interplay of ion specificity, pH and buffers: insights from electrophoretic mobility and pH measurements of lysozyme solutions. *RSC Adv.* **2013**, *3*, 5882−5888.

(72) Chen, L.; McCrate, J. M.; Lee, J. C. M.; Li, H. The role of surface charge on the uptake and biocompatibility of hydroxyapatite nanoparticles with osteoblast cells. *Nanotechnology* **2011**, *22*, No. 105708.

(73) Ge, Y.; Zhang, Y.; Xia, J.; Ma, M.; He, S.; Nie, F.; Gu, N. Effect of surface charge and agglomerate degree of magnetic iron oxide nanoparticles on KB cellular uptake in vitro. *Colloids Surf., B* **2009**, *73*, 294−301.

(74) Marquis, B. J.; Liu, Z.; Braun, K. L.; Haynes, C. L. Investigation of noble metal nanoparticleζ-potential effects on single-cell exocytosis function in vitro with carbon-fiber microelectrode amperometry. *Analyst* **2011**, *136*, 3478−3486.

(75) Limpouchová, Z.; Procházka, K. Theoretical Principles of Fluorescence Spectroscopy. In *Fluorescence Studies of Polymer Containing Systems*, Procházka, K., Ed.; Springer International Publishing, 2016; pp. 91−149.

(76) Chan, J. W.; Motton, D.; Rutledge, J. C.; Keim, N. L.; Huser, T. Raman Spectroscopic Analysis of Biochemical Changes in Individual Triglyceride-Rich Lipoproteins in the Pre- and Postprandial State. *Anal. Chem.* **2005**, *77*, 5870−5876.

(77) Otero, V.; Sanches, D.; Montagner, C.; Vilarigues, M.; Carlyle, L.; Lopes, J. A.; Melo, M. J. Characterisation of metal carboxylates by Raman and infrared spectroscopy in works of art. *J. Raman Spectrosc.* **2014**, *45*, 1197−1206.

(78) Sobanska, S.; Barbillat, J.; Moreau, M.; Nuns, N.; De Waele, I.; Petitprez, D.; Tobon, Y.; Brémard, C. Influence of stearic acid coating of the NaCl surface on the reactivity with NO2 under humidity. *Phys. Chem. Chem. Phys.* **2015**, *17*, 10963−10977.

(79) Gillies, R.; Kollias, N.; Hasan, T.; Diddens, H. Spectral characterization of the benzoporphyrin derivative monoacid ring— A photoproduct formed in fetal calf solutions during irradiation with 694 nm continuous-wave radiation. *J. Photochem. Photobiol., B* **1996**, *33*, 87−90.

(80) Lin, J.; Wang, S.; Huang, P.; Wang, Z.; Chen, S.; Niu, G.; Li, W.; He, J.; Cui, D.; Lu, G.; et al. Photosensitizer-Loaded Gold Vesicles with Strong Plasmonic Coupling Effect for Imaging-Guided Photothermal/Photodynamic Therapy. *ACS Nano* **2013**, *7*, 5320−5329.

(81) Goodman, A. M.; Neumann, O.; Norregaard, K.; Henderson, L.; Choi, M. R.; Clare, S. E.; Halas, N. J. Near-infrared remotely triggered drug-release strategies for cancer treatment. *Proc. Natl. Acad. Sci. U.S.A.* **2017**, *114*, 12419−12424.

(82) Zhao, T.; Chen, L.; Li, Q.; Li, X. Near-infrared light triggered drug release from mesoporous silica nanoparticles. *J. Mater. Chem. B* **2018**, *6*, 7112−7121.

(83) Stubbs, M.; McSheehy, P. M.; Griffiths, J. R. Causes and consequences of acidic pH in tumors: a magnetic resonance study. *Adv. Enzyme Regul.* **1999**, *39*, 13−30.

(84) Morrot, A.; da Fonseca, L. M.; Salustiano, E. J.; Gentile, L. B.; Conde, L.; Filardy, A. A.; Franklim, T. N.; da Costa, K. M.; Freire-de-Lima, C. G.; Freire-de-Lima, L. Metabolic Symbiosis and immunomodulation: How Tumor Cell-Derived Lactate May Disturb innate and Adaptive immune Responses. *Front Oncol.* **2018**, *8*, No. 81.

(85) Martin, M. M.; Lindqvist, L. The pH dependence of fluorescein fluorescence. *J. Lumin.* **1975**, *10*, 381−390.

(86) Zimmermann, A.; Ritsch-Marte, M.; Kostron, H. In Vitro Investigation on the pH Dependence of the Absorption and Fluorescence Properties of the Photosensitizer mTHPC¶. *Photochem. Photobiol.* **2002**, *75*, 335.

(87) Fischer, F.; Graschew, G.; Sinn, H. J.; Maier-Borst, W.; J Lorenz, W.; Schlag, P. M. A chemical dosimeter for the determination of the photodynamic activity of photosensitizers. *Clin. Chim. Acta* **1998**, *274*, 89−104.

(88) Bodannes, R. S.; Chan, P. C. Ascorbic acid as a scavenger of singlet oxygen. *FEBS Lett.* **1979**, *105*, 195−196.

(89) Floriano-Sánchez, E.; Villanueva, C.; Noel Medina-Campos, O.; Rocha, D.; Javier Sánchez-González, D.; Cárdenas-Rodríguez, N.; Pedraza-Chaverrí, J.; et al.*et al.* Nordihydroguaiaretic acid is a potent in vitro scavenger of peroxynitrite, singlet oxygen, hydroxyl radical, superoxide anion and hypochlorous acid and prevents in vivo ozone-induced tyrosine nitration in lungs. *Free Radical Res.* **2006**, *40*, 523−533.

(90) Yan, J.; Zhang, X.; Liu, Y.; Ye, Y.; Yu, J.; Chen, Q.; Wang, J.; Zhang, Y.; Hu, Q.; Kang, Y.; et al. Shape-controlled synthesis of liquid metal nanodroplets for photothermal therapy. *Nano Res.* **2019**, *12*, 1313−1320.

(91) Deng, X.; Guan, W.; Qing, X.; Yang, W.; Que, Y.; Tan, L.; Liang, H.; Zhang, Z.; Wang, B.; Liu, X.; et al. Ultrafast Low-Temperature Photothermal Therapy Activates Autophagy and Recovers Immunity for Efficient Antitumor Treatment. *ACS Appl. Mater. Interfaces* **2020**, *12*, 4265−4275.

(92) Pérez-Hernández, M. Mechanisms of Cell Death Induced by Optical Hyperthermia. In *Nanomaterials for Magnetic and Optical Hyperthermia Applications*, Fratila, R. M.; De La Fuente, J. M., Eds.; Elsevier, 2019; pp. 201−228.

(93) Osti, L.; Berardocco, M.; di Giacomo, V.; Di Bernardo, G.; Oliva, F.; Berardi, A. C. Hyaluronic acid increases tendon derived cell viability and collagen type I expression in vitro: Comparative study of four different Hyaluronic acid preparations by molecular weight. *BMC Musculoskeletal Disord.* **2015**, *16*, No. 284.

(94) Gallorini, M.; Berardi, A. C.; Berardocco, M.; Gissi, C.; Maffulli, N.; Cataldi, A.; Oliva, F. Hyaluronic acid increases tendon derived cell viability and proliferation in vitro: comparative study of two different hyaluronic acid preparations by molecular weight. *Muscles Ligaments Tendons J.* **2019**, *07*, No. 208.

(95) Celli, J. P.; Solban, N.; Liang, A.; Pereira, S. P.; Hasan, T. Verteporfin-based photodynamic therapy overcomes gemcitabine insensitivity in a panel of pancreatic cancer cell lines. *Lasers Surg. Med.* **2011**, *43*, 565−574.

(96) Broekgaarden, M.; Anbil, S.; Bulin, A.-L.; Obaid, G.; Mai, Z.; Baglo, Y.; Rizvi, I.; Hasan, T. Modulation of redox metabolism negates cancer-associated fibroblasts-induced treatment resistance in a heterotypic 3D culture platform of pancreatic cancer. *Biomaterials* **2019**, *222*, No. 119421.

(97) Bulin, A.-L.; Broekgaarden, M.; Hasan, T. Comprehensive high-throughput image analysis for therapeutic efficacy of architecturally complex heterotypic organoids. *Sci Rep* **2017**, *7*, No. 16645.

(98) Mallidi, S.; Watanabe, K.; Timerman, D.; Schoenfeld, D.; Hasan, T. Prediction of Tumor Recurrence and Therapy Monitoring Using Ultrasound-Guided Photoacoustic Imaging. *Theranostics* **2015**, *5*, 289−301.

(99) Xavierselvan, M.; Cook, J.; Duong, J.; Diaz, N.; Homan, K.; Mallidi, S. Photoacoustic Nanodroplets for Oxygen Enhanced Photodynamic Therapy of Cancer. *Photoacoustics* **2022**, *25*, No. 100306.

(100) Mallidi, S.; Anbil, S. R.; Lee, S.; Manstein, D.; Elrington, S. A.; Kositratna, G.; Schoenfeld, D.; Pogue, B. W.; Davis, S. J.; Hasan, T. Photosensitizer fluorescence and singlet oxygen luminescence as dosimetric predictors of topical 5-aminolevulinic acid photodynamic therapy induced clinical erythema. *J. Biomed. Opt.* **2014**, *19*, 1−13.

https://doi.org/10.1021/acsanm.1c04353
ACS Appl. Nano Mater. 2022, 5, 6125−6139